



City Research Online

City, University of London Institutional Repository

Citation: Cai, B., Li, K. & Fu, F. (2023). Theoretical analysis of the moment-curvature relationship of coal gangue concrete beams. *Proceedings of the Institution of Civil Engineers - Structures and Buildings*, pp. 1-21. doi: 10.1680/jstbu.22.00066

This is the accepted version of the paper.

This version of the publication may differ from the final published version.

Permanent repository link: <https://openaccess.city.ac.uk/id/eprint/30493/>

Link to published version: <https://doi.org/10.1680/jstbu.22.00066>

Copyright: City Research Online aims to make research outputs of City, University of London available to a wider audience. Copyright and Moral Rights remain with the author(s) and/or copyright holders. URLs from City Research Online may be freely distributed and linked to.

Reuse: Copies of full items can be used for personal research or study, educational, or not-for-profit purposes without prior permission or charge. Provided that the authors, title and full bibliographic details are credited, a hyperlink and/or URL is given for the original metadata page and the content is not changed in any way.

City Research Online:

<http://openaccess.city.ac.uk/>

publications@city.ac.uk

Theoretical analysis of the moment-curvature relationship of coal gangue concrete beam

Bin Cai¹, Kaiyi Li¹ and Feng Fu^{2*}

¹ School of Civil Engineering, Jilin Jianzhu University, Changchun 130118, Jilin, China.

² Department of Engineering, School of Science and Technology, City, University of London, London, EC1V, 0HB, United Kingdom

*Correspondence: feng.fu.1@city.ac.uk

Abstract

At present, there are fewer studies on the application of coal gangue concrete to structural components. In order to study the variation of moment-curvature relationship of steel fiber-reinforced coal gangue concrete (SFCGC) beams, a simplified calculation method of moment-curvature is proposed in this study for the calculation of moment-curvature measurements of SFCGC beams. The calculation equations of SFCGC beams were optimized based on current design codes, including theoretical calculations of flexural stiffness, crack width and spacing, cracking moment, and ultimate moment. The calculated results were compared with the experimental results to verify that the cracking moment and ultimate moment of SFCGC beams are slightly lower than those of natural concrete (NC) beams, but the cracking moment, flexural stiffness, and ductility of SFCGC beams can be increased by incorporating steel fibers. And increasing the rebar ratio can significantly improve the load-carrying capacity of SFCGC beams but will reduce the ductility. The calculated value has a small error with the experimental value, which proves that the optimized design specification formula has a high

23 calculation accuracy and is applicable to the design of the bending behavior of SFCGC beams. This
24 provides a theoretical basis for the subsequent related research.

25 **Keywords:** Steel fiber reinforced coal gangue concrete beam; Moment-curvature; Crack width;
26 Cracking moment; Ultimate moment

27 **1. Introduction**

28 Coal gangue is a by-product of coal mining and raw coal processing. The accumulation of its
29 waste significantly threatens the health and safety of the human population, as well as the ecological
30 health of the environment (Gong et al. 2016). To date, approximately 4.5 billion tons of coal gangue
31 waste has been generated from the process of coal mining in China and continues to grow at a rate of
32 150-200 million tons per year. Meanwhile, however, the large-scale urbanization construction efforts
33 in China have caused the mining rate of natural sand and gravel to exceed the natural recovery rate of
34 these materials. Coal gangue, with its stable structure and low reactivity, needs to be activated via
35 mechanical grinding and thermal and chemical activation methods before it can be used in construction
36 applications (Guo et al. 2016; Li et al. 2013). By testing the basic physical and mechanical properties
37 of coal gangue aggregate, Wang and Zhao (2015) showed that coal gangue can meet the requirements
38 of compressive strength of concrete aggregate. Through the mechanical property test of coal gangue
39 concrete without steel fiber, Zhu et al. (2020) found that when the coal gangue replacement rate is
40 more than 50%, it will lead to a rapid decrease in its compressive strength. Under standard curing
41 conditions, coal gangue addition reduced the early strength of concrete, increased porosity and water
42 absorption, but improved resistance to chloride ions or gas permeability. Using coal gangue instead of
43 gravel to make concrete can simultaneously consume a large amount of coal gangue (Karimaei et al.
44 2020) and reduce the use of gravel in the construction industry. This method holds a significant impact

45 on the development of eco-friendly building materials and the reduction of industrial energy
46 consumption and ultimately, to protect the natural environment (Wu et al. 2018; Moghadam et al. 2019;
47 Qin et al. 2019). For example, Sun and Li (2011) developed coal gangue concrete for gob-side entry
48 retaining, which not only solve the problem of ecological environment and resource shortage, but also
49 reduce the cost of filling material and increase the economic benefit of coal mine enterprise. Besides,
50 the coal gangue also could be used as inexpensive adsorbent in industrial wastewater pretreatment
51 (Jabłońska et al. 2020). And self- self-ignited gangue can also be recycled as a partial substitute for
52 Portland cement and reduce the carbon footprint of fossil fuels in order to protect the environment
53 (Qin and Gao 2019). In recent years, scholars around the world have conducted extensive experimental
54 and theoretical research on the mechanical properties of coal gangue concrete. Jin-min (2011) found
55 that when the proportion of coal gangue replacement gravel is less than 30%, the working capacity of
56 concrete is relatively stable; with the increasing amount of coal gangue replacement, the working
57 capacity of concrete decreases; with the increasing amount of coal gangue replacement, the apparent
58 density of concrete increases continuously. Guo and Zhu (2011) used orthogonal test and
59 comprehensive balance method to analyze the durability of coal gangue concrete to determine the best
60 ratio of coal gangue concrete. Zhang (2020) found that the addition of spontaneous combustion coal
61 gangue aggregate significantly affects the mechanical properties of concrete, reducing the compressive
62 strength, splitting tensile strength, and elastic modulus. Ma (2020) concluded that the concrete mixed
63 with calcined coal gangue has good sulfate resistance. As coarse aggregate, coal gangue has high
64 compressive strength and durability in alkali-activated coal gangue-slag concrete and can be used in
65 chemical erosion environments such as chloride or sulfate. Gao (2021) proposed constants for
66 predicting the splitting tensile strength and elastic modulus of coal gangue concrete. In addition, Liu

67 (2020) further proposed a new model to accurately estimate the elastic modulus of spontaneous
68 combustion coal gangue concrete by considering the replacement rate, compressive strength, and
69 density of the concrete. However, there have been relatively few studies on coal gangue components.

70 Invented in 1874, steel fiber-reinforced concrete has been a useful structural material since the
71 1970s (Katzner and Domski 2012), as the addition of steel fibers considerably improves the mechanical
72 properties of concrete, including its impact strength, toughness, flexural and tensile strength, ductility,
73 and resistance to cracking and spalling (Mohammadi et al. 2008). Although steel fibers have been
74 increasingly used in structures such as building floors, prefabricated elements, tunnels, heavy-duty
75 pavements, and mining structures (Atis and Karahan 2009, Wang et al. 2020), nonetheless this
76 composite material still requires extensive research (Brandt 2008; Olivito and Zuccarello 2010). The
77 fibers can effectively retard the appearance and development of microcracks in the concrete matrix
78 and help improve the toughness, ductility and bending properties of UHPC and avoid brittle damage
79 (Chen et al. 2019). And the aspect ratio and volume fraction of steel fibers have significant effects on
80 the workability of steel fiber composites (Yazıcı 2007). The aspect ratio is generally between 50 and
81 100. As the l/d increases, the uneven distribution of fibers in the concrete mix and the probability of
82 flocculation increase. The most suitable volume fraction of steel fibers is 0.5%-2.5% (Yazıcı 2007).
83 The existence of voids in the bond between coal gangue and cement mortar compromises the
84 compressive strength and durability of concrete and has the disadvantages of high porosity and strong
85 water absorption (Ma et al. 2018). Therefore, steel fibers can be added to coal gangue concrete to
86 enhance its performance and increase its suitability for construction.

87 In the field of theoretical research on the moment-curvature relationship and the calculation of
88 deflection, Wu et al. (2021) developed an iterative algorithm to calculate the deflection of unbonded

89 FRP tendon prestressed beams. The Babilio and Lenci (2017) study obtained uncoupled linear
90 approximation provides an indication of a more suitable curvature definition. Kwak and Kim (2002)
91 performed a material nonlinear analysis of reinforced concrete beams considering tensile softening
92 branching and bond slip. The control equations describing the bond-slip behavior in the beam are
93 derived, which simplifies the finite element modeling and analysis process and effectively describes
94 the bond-slip behavior. And the developed algorithm is also reflected in the bending moment-curvature
95 relationship of the RC section. Hadhood (2018) established the moment-curvature relationship for full-
96 scale circular FRP-RC members by means of a validated layer-by-layer analytical model. Viet and
97 Zaki (2019) first developed mathematical formulations to predict and describe the internal material
98 structure of the composite considering the solid phase transition of SMA bars. Then the analytical
99 expression of the bending moment-curvature relationship is obtained. Foroughi and Yüksel (2020)
100 obtained the moment-curvature relationship of reinforced concrete square columns in SAP2000
101 software by considering the nonlinear properties of the material. Priestley et al. (1971) derived the
102 bending moment relationship for prestressed concrete members using a purely analytical approach,
103 including the effect of concrete tension between cracks. Hasan et al. (2019) developed a numerical
104 integration method to study moment-curvature behavior of circular normal strength concrete (NSC)
105 and high strength concrete (HSC) columns reinforced with (GFRP) rods.

106 Concrete with coal gangue as coarse aggregate can turn waste into treasure, resolve the problem
107 of environmental pollution caused by the accumulation of coal gangue, and improve economic and
108 ecological benefits, which is in line with the concept of national sustainable development. Flexural
109 performance is an important characteristic of reinforced concrete members. For the theoretical
110 calculation of the flexural performance of concrete beams in this aspect of research, Du et al. (Du et

111 al. 2021) carried out a theoretical analysis of the flexural performance of alkali-activated concrete
112 beams. And Jia et al. (Jia et al. 2021) carried out a theoretical analysis of the flexural performance of
113 concrete beams with the coarse aggregate post-filling process. But at present, there is no relevant
114 theoretical analysis of the flexural performance of steel fiber reinforced gangue concrete beam, which
115 has brought inconvenience to the application of engineering structural designers. In this paper, based
116 on the four-point bending test of SFCGC beams, with coal gangue replacement rate, steel fiber volume
117 content (SFVC), rebar ratio, and beam height as the parameter variables, the curvature, the cracking
118 moment, ultimate bending moment, flexural stiffness and crack spacing and width of SFCGC beams
119 are theoretically analyzed. The flexural performance of the SFCGC beams was investigated and
120 verified using the current structural code, demonstrating the applicability of the current provisions to
121 the design of SFCGC beams. The test results and findings provide theoretical support for the
122 popularization and application of coal gangue.

123 **2. Test Materials**

124 2.1. Materials

125 The appearance of the coal gangue is shown in Fig. 1(a). The chemical composition of coal
126 gangue was determined by X-ray fluorescence spectroscopy (XRF) completed at Jilin University. The
127 results are shown in Table 1. As shown in Table 1, the contents of SiO_2 and Al_2O_3 in coal gangue are
128 higher, 48.14% and 16.48%, respectively. Si and Al are the main components of coal gangue chemical
129 composition, and the change of its structure level in the activation process is the key to affecting the
130 strength of coal gangue composite cement. It is known that coal gangue can be used as concrete coarse
131 aggregate (Li et al. 2006). Corrugated steel fibers were used, as shown in Fig. 1(b). By the physical
132 property test performed at Jilin Jianzhu University, the specific physical properties of the raw materials

133 used to prepare SFCGC specimens are shown in Table 2.



134

(a) Coal gangue

(b) Steel fiber

135

136

Fig. 1. Appearance of the materials.

137 Table 1

138 Chemical composition of the coal gangue.

SiO ₂	Al ₂ O ₃	Fe ₂ O ₃	FeO	BaO	MgO	K ₂ O	Na ₂ O	TiO ₂	P ₂ O ₅	MnO
48.14	16.48	4.59	7.03	7.40	6.53	2.16	3.70	2.31	0.51	0.2

139 Table 2

140 Materials for the experimental study.

Materials	Information
Cement	P.O42.5 ordinary Portland cement of Changchun Cement Co., Ltd; initial setting time: 90min; final setting time: 265min; compressive strength: 24.9Mpa(3days) and 48.7Mpa(28days); specific surface area: 344m ² /kg; loss on ignition: 2.6%
Sand	River sand; the fineness modulus: 2.8; and the bulk density: 1450kg/m ³
Stone	Ordinary gravel; size gradation: 5–25mm; bulk density: 1500kg/m ³ ; and crushing

	index:7%
Coal	Size gradation: 5–25mm; bulk density: 1206kg/m ³ ; water absorption: 8.3%; and
gangue	crushing index: 18%
Water	Ordinary tap water
Plasticizer	The rate of water reduction: 20%; fineness: 0.315mm, and the major component: Sodium β -Naphthalene Sulfonate
Steel fiber	Undulated steel fiber (Fig. 1(b)), 38mm long, 1mm wide, and 0.35-0.5mm thick, aspect ratio: 50, and density: 7850kg/m ³

141

142 2.2. SFCGC mixtures

143 Six mixing ratios were used for experimental testing, as shown in Table 3. The first and second
144 numerals in the designation of each specimen denote the coal gangue replacement rate (0%, 50%,
145 100%) and the SFVC (0%, 0.5%, 1%, 1.5%), respectively. The dimensions and quantities of coal
146 gangue specimens were determined according to the provisions given by GB/T 50081-2019 (CABR
147 2019). Specifically, three test blocks of each with a dimension of 150 mm \times 150 mm \times 150 mm and
148 one test block with a dimension of 100 mm \times 100 mm \times 300 mm were cast for each mixing ratio.
149 Uniaxial compression and splitting tensile tests were performed using a Type YAR-2000
150 electrohydraulic servo universal testing equipment in accordance with GT50081-2019 (CABR 2019)
151 as shown in Fig. 2(a)-(b), similar equipment can be seen in Fu (2010,2018), Gao (2017) ,Qian
152 (2022,2020),The cube axial compressive strength (f_{cu}) and splitting tensile strength (f_t) of concrete
153 were obtained from these two tests respectively. And the axial compressive strength of prisms (f_c) and
154 the concrete modulus of elasticity of concrete (E_c) is obtained by uniaxial compression testing of

155 prisms as shown in Fig. 2(c). The results provide data to support the subsequent theoretical analysis,

156 as shown in Table 3.



157

158 (a) Cubic axial compression resistance test (b) Cube splitting tensile test (c) Prismatic axial

159 compression test

160 Fig. 2. Test setup for mechanical properties of concrete.

161 Table 3

162 Mixture compositions.

Unit:kg/m³

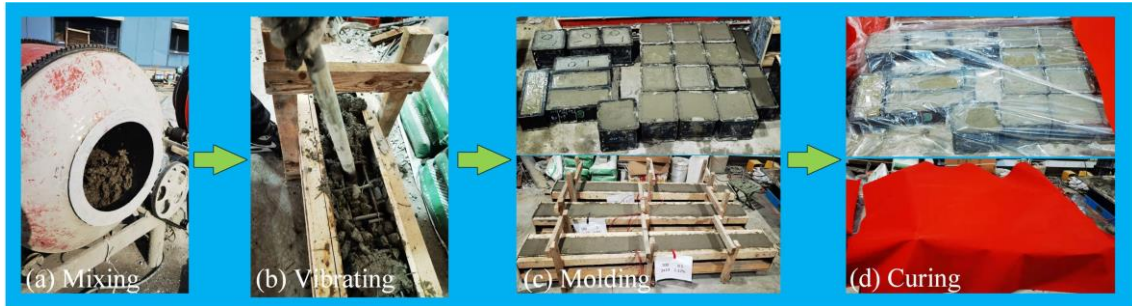
No.	R%	V _{sf} %	Cg	gravel	cement	sand	Pl	W/C	f _{cu} /Mpa	f _c /Mpa	f _i /Mpa	E _c /Gpa
M0-1	0	1	0	1155.5	503.7	622.22	5.04	0.40	47.11	36.23	3.53	34.05
M50-1	50	1	577.7	577.8	503.7	622.22	5.04	0.40	46.62	35.45	3.51	33.96
M100-0	100	0	1155.5	0	503.7	622.22	5.04	0.40	35.87	25.67	2.44	29.79
M100-0.5	100	0.5	1155.5	0	503.7	622.22	5.04	0.40	42.31	32.39	2.88	33.11
M100-1	100	1	1155.5	0	503.7	622.22	5.04	0.40	46.56	34.58	3.48	33.95
M100-1.5	100	1.5	1155.5	0	503.7	622.22	5.04	0.40	46.83	34.81	3.61	34.02
M100-2	100	2	1155.5	0	503.7	622.22	5.04	0.40	46.82	34.69	3.62	34.00

163 Note: R = the coal gangue replacement rate; V_{sf} = the SFVC, CG = the coal gangue coarse aggregate;

164 Pl = the plasticizer; W/C = the water-cement ratio.

165 2.3. SFCGC preparation

166 In accordance with the provisions given by GB/T 50080-2002 (CABR 2003), Qiant(2020,2021),
 167 the concrete specimens were prepared using a mortar stone wrapping method with a dry-wet mixing
 168 process (Gao 2017). Fig. 3 shows the process of making the specimens.



169

170 Fig. 3. The specimen fabrication process.

171 2.4. Specimen parameters

172 To investigate the influence of R , V_{sf} , and ρ on the moment-curvature relationship of SFCGC
 173 beams, a total of ten SFCGC beams and two natural concrete (NC) beams were designed. The specific
 174 parameters of the experimental beams are shown in Table 4. The concrete cover of each specimen had
 175 a thickness of 25 mm. The detailing and cross-sections of the beams refer to Cai's tests (Cai et al.
 176 2023), and the basic properties of the rebar used in the specimens obtained from Cai's tests (Cai et al.
 177 2023).

178 Table 4

179 Design of the test beams.

Specimens	b/mm	h/mm	h_0/mm	L/mm	L_0/mm	$R\%$	$V_{sf}\%$	$\rho\%$
N2-0-1	150	200	175	2000	1800	0	1	1.17
S1-100-1	150	200	175	2000	1800	100	1	0.6

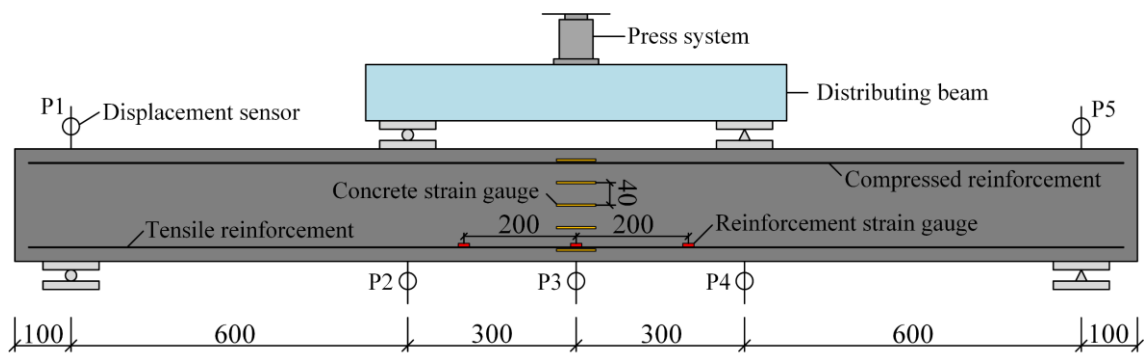
S2-100-1	150	200	175	2000	1800	100	1	1.17
S3-100-1	150	200	175	2000	1800	100	1	1.94
S2-50-1	150	200	175	2000	1800	50	1	1.17
S2-100-0	150	200	175	2000	1800	100	0	1.17
S2-100-0.5	150	200	175	2000	1800	100	0.5	1.17
S2-100-1.5	150	200	175	2000	1800	100	1.5	1.17
S2-100-2	150	200	175	2000	1800	100	2	1.17
N4-0-1	150	300	275	2000	1800	0	1	1.12
S4-50-1	150	300	275	2000	1800	50	1	1.12
S4-100-1	150	300	275	2000	1800	100	1	1.12

180 Note: b = beam section width; h = beam section height; h_0 = the effective height; L = beam length; L_0
181 = beam effective length; ρ = the rebar ratio. In the specimen names, the first symbol indicates the type
182 of materials, S = SFCGC, N = NC; the second symbol indicates ρ ; the numeral “1, 2, 3, 4” indicates
183 0.6%, 1.17%, 1.94%, 1.12%, respectively; the third symbol indicates R ; and the fourth symbol indicates
184 V_{sf} .

185 2.5. Test loading Scheme

186 A 500-kN hydraulic servo pressure testing machine was used in the test. As shown in Fig. 4, a
187 four-point bending test was performed with two-point symmetrical loading. The pure bending region
188 of the beam had a length of 600 mm. According to GB/T 50152-2012 (CABR 2011), force-controlled
189 loading was adopted in this test. Before formal loading, a preload of 5 kN was applied to ensure the
190 normal operation of the equipment. After preloading, the load was zeroed, and formal loading began
191 at a rate of 2 kN/min. At each level, the cumulative load was 5 kN and was held for 5 min, during

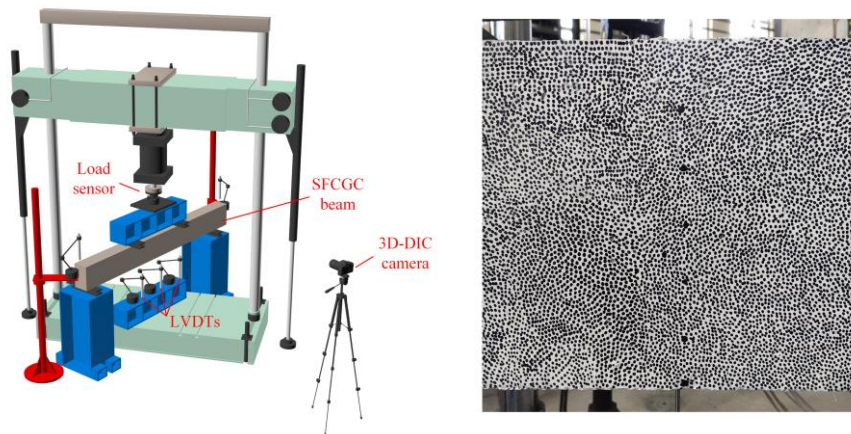
192 which crack width was recorded using a crack width gauge. After steel rebar yielding, the load was
 193 applied continuously at a reduced rate of 1 kN/min and an increment of 2 kN at each level until
 194 specimen failure. To obtain changes in the transverse strain of the concrete, the concrete strain was
 195 measured on both sides of the beam: on one side a traditional strain gauge method was used, and on
 196 the other side, a DIC technique was used. Digital Image Correlation (DIC) is a non-contact
 197 measurement technique that can be used to track the full-field strain and displacement of deforming
 198 objects (Schreier et al. 2009). The test system is shown in Fig. 5.



199

200

Fig. 4. Test setup of beam specimens.



201

202

(a) DIC test instrument

(b) Beam speckle pattern

203

Fig. 5. DIC test preparation.

204 3. Experimental phenomena and results

205 3.1. Experimental phenomena

206 The load-mid-span deflection curve (Cai et al. 2023) and crack development pattern (Fig. 6) of
207 the SFCGC beams were similar to those of the NC beams. Some of the data in Fig. 6 are sourced from
208 Cai's study (Cai et al. 2023). When the load reached $0.3F_u$ (where F_u is the ultimate load), 1-3 vertical
209 cracks with a width generally < 0.02 mm initially appeared in the region near the loading point in the
210 pure bending section. Distribution of concrete strains along the height of the specimen is obtained
211 from Cai's study (Cai et al. 2023). When the SFCGC beams cracked, the component's deflection
212 increased. At the same time, the concrete and rebar strain readings changed to some extent. Under all
213 levels of load, the strain of each point on the normal section of concrete in the tension area is
214 approximately proportional to the distance from the point to the neutral axis. Nonetheless, they still
215 met the plane-section assumption. This proves that the SFCGC beam has a stable bending bearing
216 capacity. When the load increased to $0.5F_u$, new cracks in the pure bending section no longer appeared,
217 and the cracks propagated along the direction of the compression zone. Compared with the NC beam,
218 the crack development of the SFCGC beam is faster due to the porous structure of coal gangue
219 aggregate, but the crack development rate of the SFCGC beam can be slowed down by adding steel
220 fiber. At the same time, the deflection of the beam gradually increased. The neutral axis of the beam
221 moved upward, but the crack width did not increase significantly. As the load further increased to 0.8-
222 $0.85F_u$, the rebar yielded, the deflection of the beam specimen increased rapidly, and the cracks
223 continuously extended and widened. Finally, the concrete in the compression zone was crushed, as
224 shown in Fig. 6. No sliding failure occurred at the composite interface of any specimens.

225



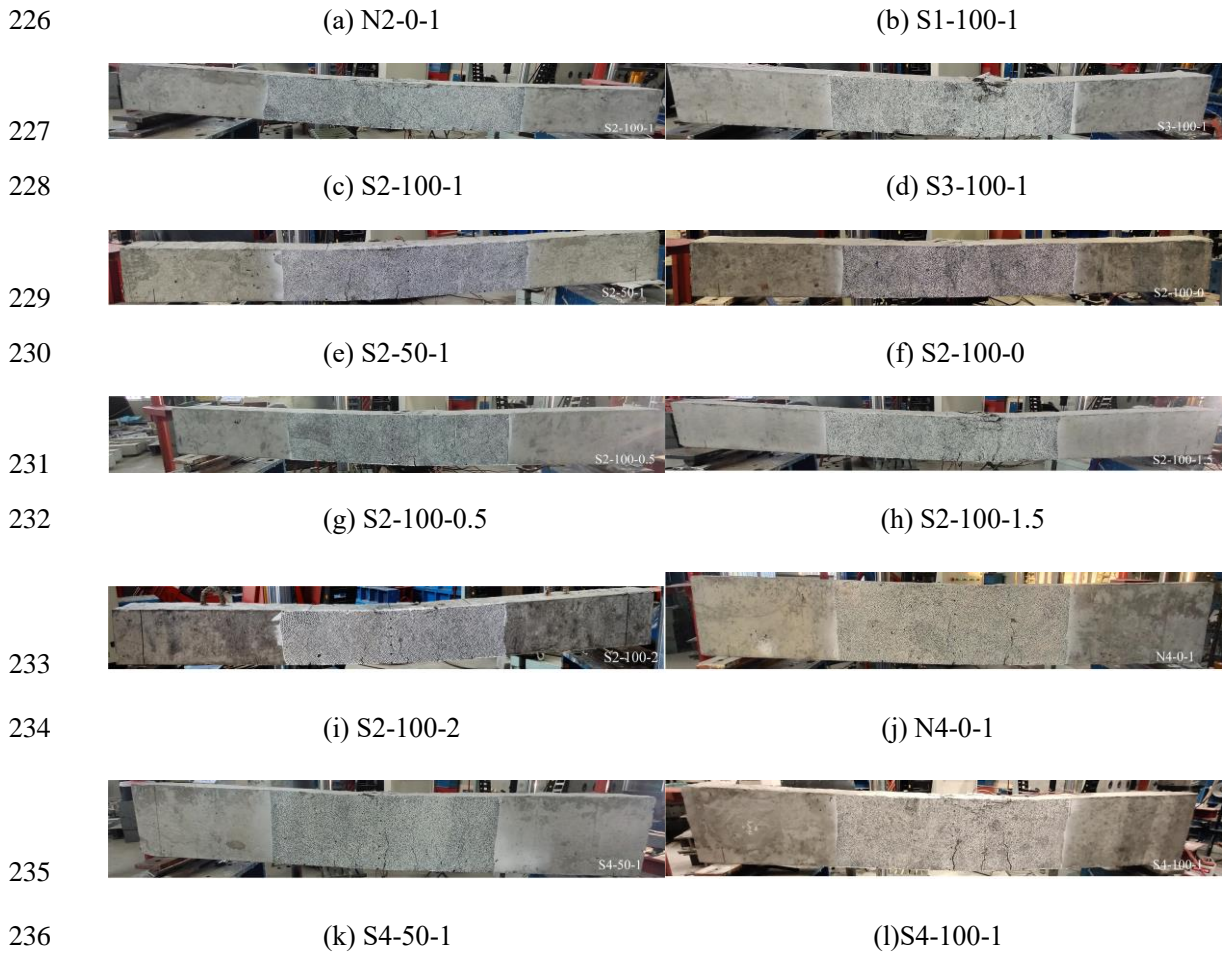
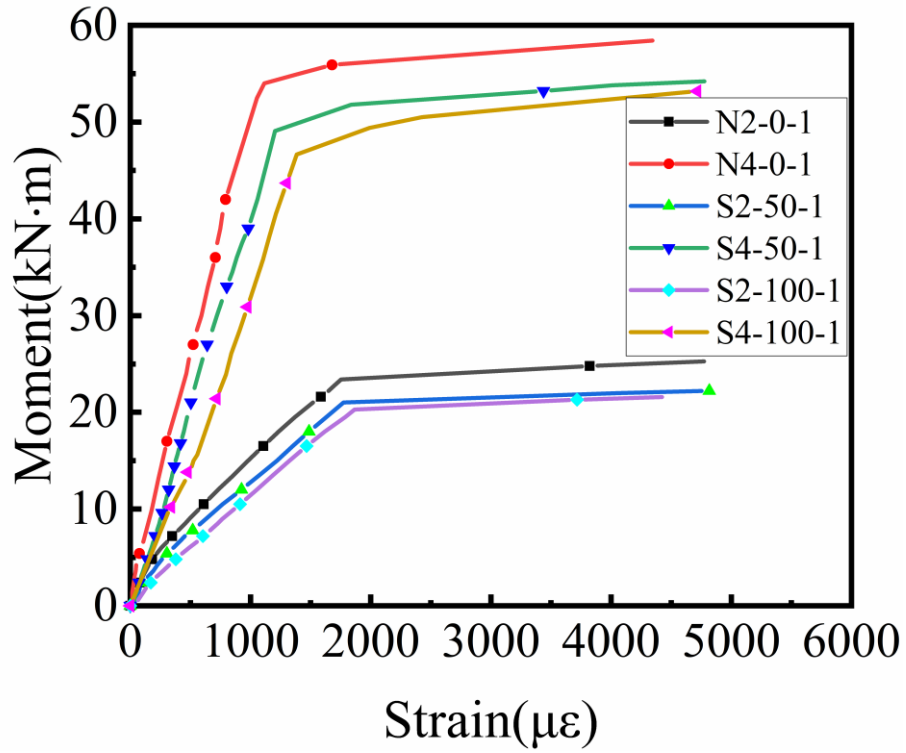


Fig. 6. Loaded state of the specimens.

3.2. Strain of longitudinal bars

Fig. 7 demonstrates the moment-rebar strain relationship in the span of the beam specimen. The moment increases gradually as the longitudinal rebar starts to yield. Similar to the moment-curvature relationship, the rebar ratio and beam depth have an important effect on the bending performance. Table 5 compares the yielding moments determined from the moment-curvature relationship and the moment-rebar strain relationship. The ratio of these two results was between 0.96-1.06, indicating that the errors in these two results were small.



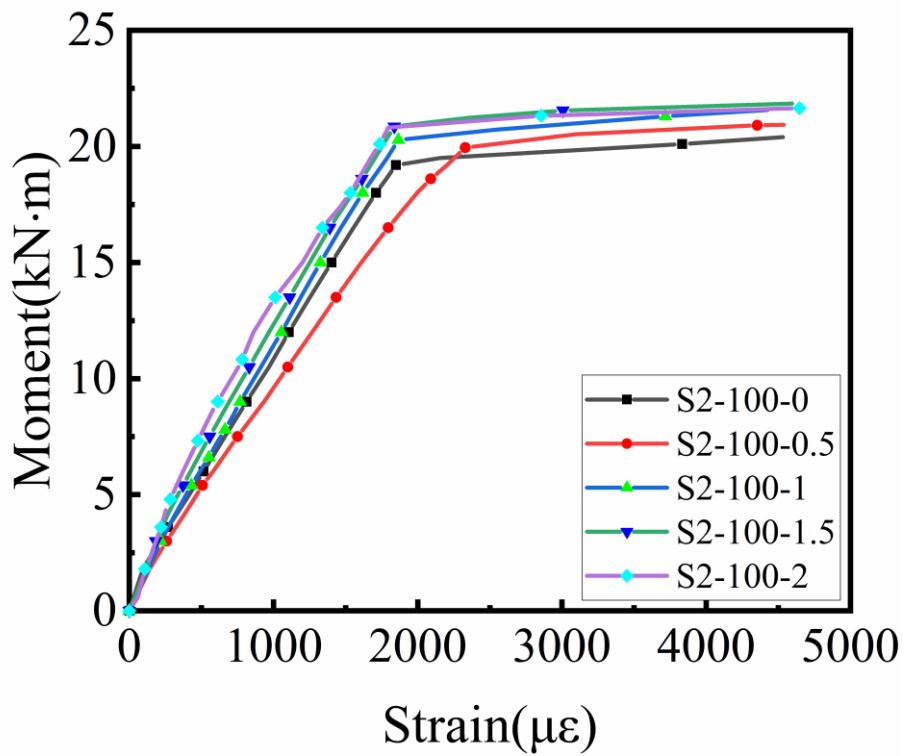
245

246

(a) Effect of coal gangue replacement rate on the moment-rebar strain relationships of the

247

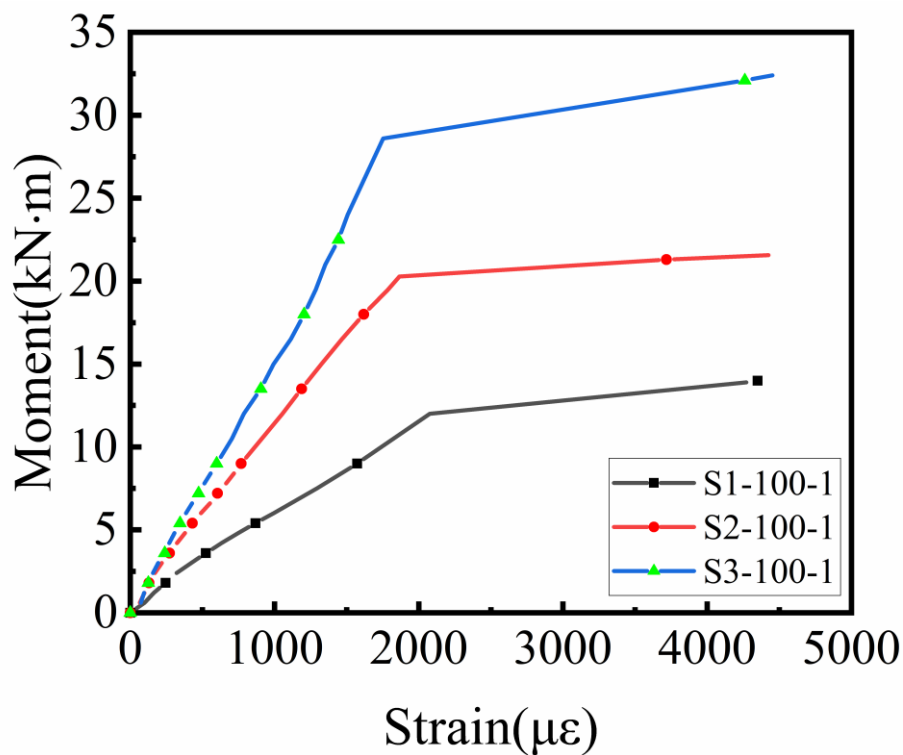
beams



248

249

(b) Effect of SFVC on the moment-rebar strain relationships of the beams



250

251

(c) Effect of rebar ratio on the moment-rebar strain relationships of the beams

252

Fig. 7. Moment-rebar strain relationships.

253 Table 5

254 Comparison of yield moments.

Specimens	M_y (kN.m)	M_{y-s} (kN.m)	M_y/M_{y-s}
N2-0-1	22.80	23.40	0.97
S1-100-1	12.74	12.00	1.06
S2-100-1	19.88	20.28	0.98
S3-100-1	27.14	28.61	0.95
S2-50-1	20.20	21.05	0.96
S2-100-0	19.50	19.20	1.02
S2-100-0.5	19.82	19.95	0.99

S2-100-1.5	20.12	20.85	0.96
N4-0-1	52.33	54.00	0.97
S4-50-1	50.44	49.08	1.03
S4-100-1	48.00	46.65	1.03

255 Note: M_y = the yield moment determined by the moment-curvature curve; and M_{y-s} = the yield moment
256 determined by the moment-rebar strain curve.

257 3.3. Crack distribution and failure mode

258 The distribution, width, and spacing of cracks are very important parameters when evaluating the
259 stress state of a beam. Fig. 8 shows the distribution of cracks in the beam specimens at the end of the
260 test. Each numeral in the figure represents the applied load (unit: kN) when the crack developed to
261 that position. Flexural cracks were generated in the pure bending region. As the load increased, new
262 cracks appeared continuously, and existing cracks propagated upward. After the load reached a certain
263 level, diagonal cracks developed along the shear span. Fig. 8 shows that as the rebar ratio increased,
264 the number of flexural cracks in the SFCGC beams increased, and the average crack spacing was
265 smaller. Additionally, for the same rebar ratio, the average crack spacing in the SFCGC beams was
266 smaller than that in the NC beams. This result indicates that the SFCGC beams exhibited a better bond
267 strength between the longitudinal rebar and the concrete. However, the beam depth did not affect the
268 crack distribution. Table 10 reports the crack width of the beams at stages $0.5 M_u$, $0.6 M_u$, and $0.7 M_u$.
269 These data show that as the SFVC increased, the crack width of the SFCGC beams decreased by 19%,
270 23%, and 13% on average at the three moments, respectively, due to the crack-arresting effect of the
271 steel fibers.

272 As shown in Fig. 8, the failure mode of the SFCGC beams was similar to that of the NC beams.

273 After the longitudinal rebar yielded, with the further increase of load, the concrete at the top of the
 274 mid-span produced transverse cracks with a crackling sound, with the main cracks in the pure bending
 275 region developing rapidly. The crushing range of the concrete at the top of the beam is small as shown
 276 in Fig. 8. Ductile failure occurred in the beam. Thus it can be seen that the failure mode of the SFCGC
 277 beam can be judged by whether or not the rebar yields when the beam specimen is destroyed. When
 278 the failure of the beam begins with the yield of the rebar and ends with the failure of the compression
 279 zone, ductile failure occurs.

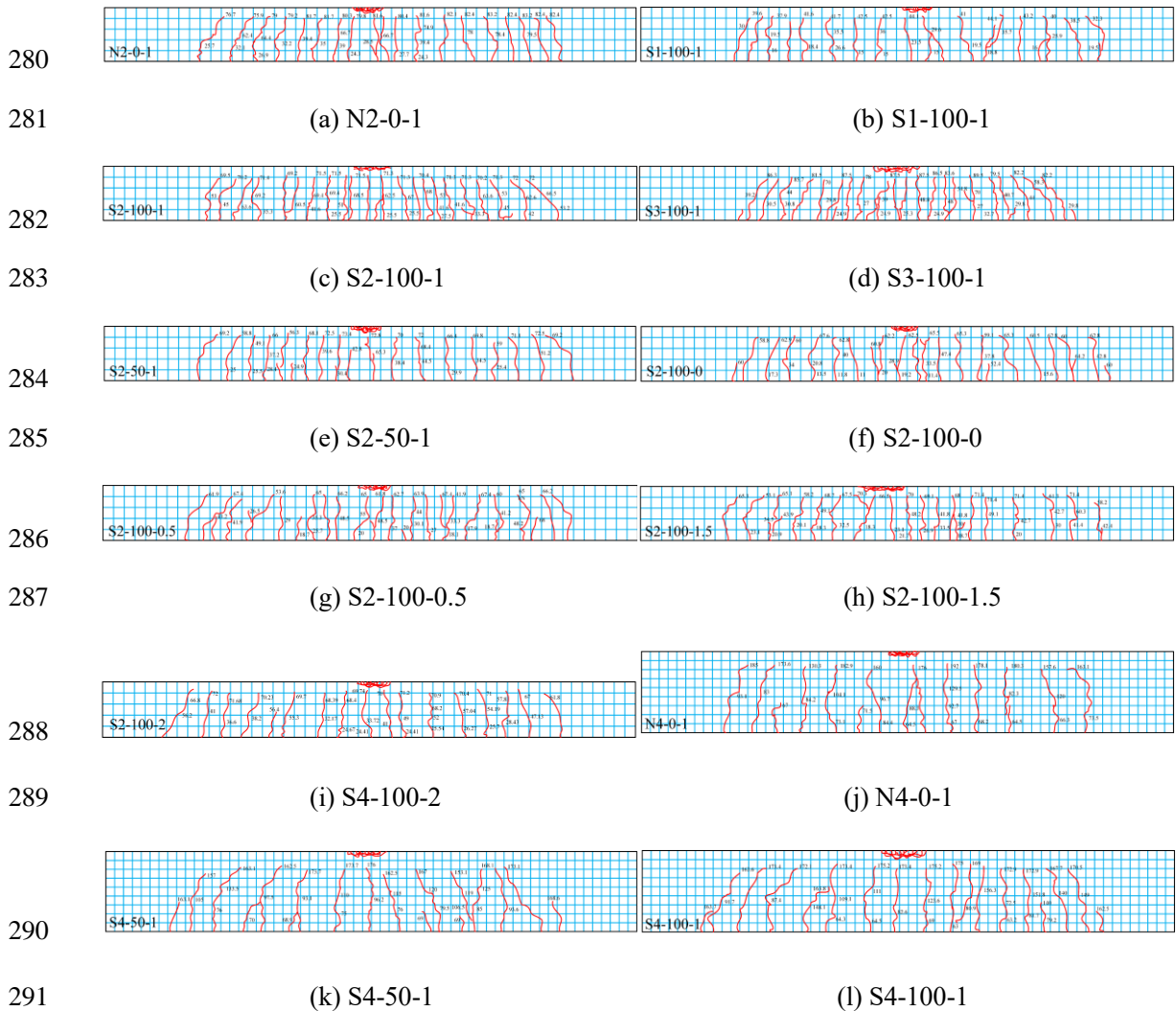


Fig. 8. Crack distribution and failure mode.

293 4. Theoretical analysis

294 4.1. Moment-curvature relationship

295 According to the knowledge of material mechanics, a beam subjected to vertical load has a
296 bending curvature whose mathematical significance is equal to the second-order differential of the
297 vertical displacement w with respect to x , while the physical significance of the curvature is the
298 reciprocal of the radius of the bending shape (Babilio and Lenci 2017). A sketch of the beam
299 deformation is shown in Fig. 9, where w is the deflection of the specimen and θ is the angle of rotation
300 of the specimen, and the following assumptions are followed:

- 301 • Plane sections remain plane under bending so that the strain in the concrete and reinforcement
302 is proportional to the distance from the neutral axis.
- 303 • The stresses at the centroid of each strip are assumed constant throughout its thickness.
- 304 • A perfect bond exists between the reinforcement and surrounding concrete.
- 305 • The tension strength of concrete is neglected

306 Let the curve be $y=f(x)$, as shown in Fig.10, and according to the mathematical principle, the
307 following relationship is obtained:

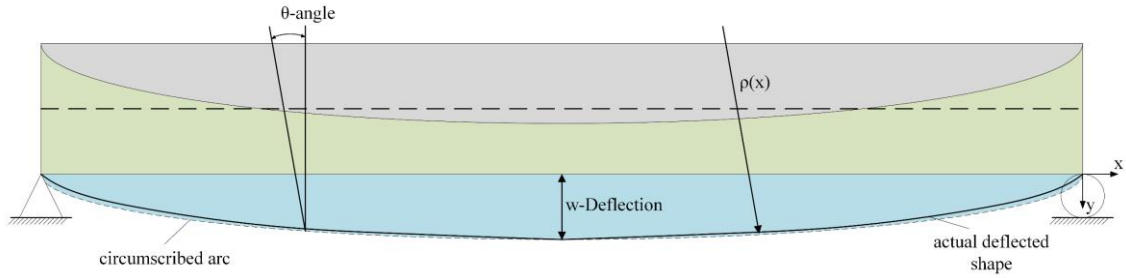
$$308 \quad \theta = \arctan y' \quad (1)$$

$$309 \quad \frac{ds}{dx} = \frac{\Delta s}{\Delta x} = \sqrt{1 + y'^2} \quad (2)$$

310 where: Δs is the curve arc length increment; and θ is the tangent line of the point and the horizontal
311 coordinate axis of the angle increment (i.e., $\theta = \beta - \alpha$).

312 According to the definition of curvature (k) and the underlying mathematical theory it is known:

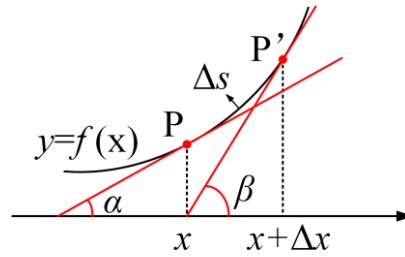
$$313 \quad k = \left| \frac{d\theta}{ds} \right| = \left| \frac{\frac{d\theta}{dx}}{\frac{ds}{dx}} \right| = \left| \frac{\frac{y''}{1 + y'^2}}{\sqrt{1 + y'^2}} \right| = \pm \frac{y''}{(1 + y'^2)^{3/2}} \quad (3)$$



314

315

Fig. 9. Actual and assumed beam deflected shapes.



316

317

Fig. 10. Curvature calculation model.

318 Based on the above derivation, the curvature of the beam specimen is shown in Equation (4):

319

$$\phi = k = \frac{1}{\rho(x)} = \frac{d^2w}{dx^2} = \pm \frac{w''}{(1+w'^2)^{3/2}} \quad (4)$$

320 According to the plane section assumption, to simplify the calculation of curvature, the bending

321 deformation curve (ACB) of the beam is approximated as a quadratic parabolic, and the calculation

322 sketch is shown in Fig. 11. Its deformation curve equation is set as shown in Equation (5). By

323 substituting the boundary conditions of A(0,0), C(a/2,-f), and B(a,0), the equation of the parabolic is

324 obtained as shown in Equation (6), and then the quadratic derivative of the equation to obtain the final

325 curvature calculation formula as shown in Equation (7). Due to the need for more accurate curvature

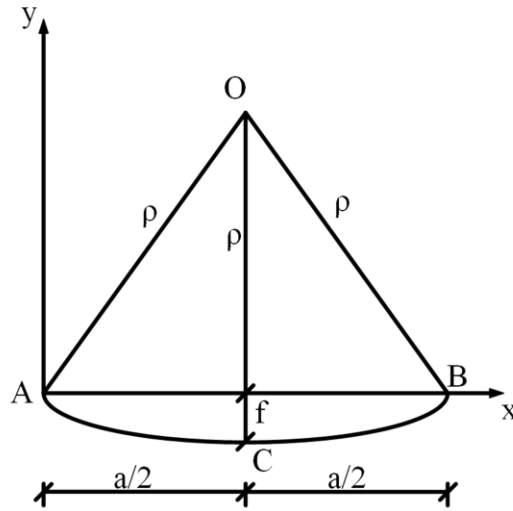
326 measurement calculation, three measurement points are arranged in the pure bending area of the beam

327 specimen (Fig. 4), and the bending curvature of the beam is calculated by calculating the difference

328 between the displacement in the span and the average displacement on the left and right sides, and the

329 formula is shown in Equation (8). This method allows the curvature of the beam to be obtained by

330 directly measuring the displacement of the beam specimen, thus avoiding the less convenient
 331 traditional method of obtaining the curvature of the beam specimen by measuring the concrete strain
 332 and the steel strain.



333

334

Fig. 11. Curvature of beam simplified calculation model.

335

$$y = c_1 x^2 + c_2 x + c_3 \quad (5)$$

336

$$y = \frac{4f}{a^2} x^2 - \frac{4f}{a} x \quad (6)$$

337

$$y'' = \frac{1}{\rho} = \frac{8f}{a^2} \quad (7)$$

338

$$\phi_t = \frac{8}{a^2} \left(f_3 - \frac{f_2 + f_4}{2} \right) \quad (8)$$

339 where c_1, c_2, c_3 are the coefficients of the quadratic parabolic equation; $f_2, f_3,$ and f_4 are the readings of
 340 displacement gauges P2, P3, and P4 in Fig. 4, respectively; and a is the spacing of displacement gauges
 341 P2 and P4.

342 Table 6 shows the flexural stiffness of the specimen, which is obtained from the slope of the
 343 moment-curvature curve at each point in time. Table 7 lists the bending moments of the beam
 344 specimens at each stage. Table 8 shows the ductility coefficient (μ) (i.e., $\mu = \phi_u / \phi_y$) of each beam, which
 345 reflects the deformation capacity of the beam specimen.

346 Fig. 12 shows that the moment-curvature curves of the SFCGC and NC beams were almost the

347 same. The curve of each beam from the initial stress state to the failure state can be divided into three
348 stages. In the first stage, the moment increased linearly; then, when the moment had increased to the
349 cracking moment, cracks appeared at the bottom of the beam, which reduced the beam's flexural
350 stiffness. In the second stage, as the moment continued to increase, the crack width increased, and the
351 cracks propagated upward. The curvature increased significantly after the longitudinal rebar yielded.
352 Eventually, the beam specimen failed due to the concrete being crushed in the compression zone. The
353 ductile failure which occurred in the specimen is in accordance with the failure law of concrete beam.

354 Fig. 12(a) shows the moment-curvature relationships of beams under different coal gangue
355 replacement rates. At the same moment level, the curvature of the beams increases with the increase
356 in the coal gangue replacement rate. The cracking moment of the beam decreases with the increase in
357 the coal gangue replacement rate but does not change significantly (enlarged version of Fig. 12(a)).

358 Fig. 12(b) shows the moment-curvature relationships of beams with different steel fiber volume
359 content. At the same moment level, the curvature of the SFCGC beams decreases with the increase in
360 SFVC, but the magnitude is smaller. The cracking moment of the SFCGC beams increases with the
361 increase in SFVC, and the magnitude is larger (enlarged version of Fig. 12(b)) because the steel fibers
362 in the tensile zone after cracking can continue to bear a portion of the stress, increasing the stiffness
363 of the cross-section after cracking.

364 Fig. 12(c) shows the moment-curvature relationships of the beams with different rebar ratios. At
365 the same moment level, the curvature of the SFCGC beams decreases with increasing rebar ratio. The
366 cracking moment of the SFCGC beams increases with increasing rebar ratio and the magnitude is
367 larger (enlarged version of Fig. 12(c)).

368 Table 6

369 Comparison of flexural stiffness.

Specimens	B_{cr}		$B_{s0.5}$		$B_{s0.6}$		$B_{s0.7}$					
	$(\times 10^{12} \text{N} \cdot \text{mm}^2)$		$(\times 10^{12} \text{N} \cdot \text{mm}^2)$		$(\times 10^{12} \text{N} \cdot \text{mm}^2)$		$(\times 10^{12} \text{N} \cdot \text{mm}^2)$					
	B_{exp}	B_{theo}	$B_{exp}/$ B_{theo}	B_{exp}	B_{theo}	$B_{exp}/$ B_{theo}	B_{exp}	B_{theo}	$B_{exp}/$ B_{theo}			
N2-0-1	3.11	2.90	1.07	1.81	1.63	1.11	1.60	1.56	1.03	1.55	1.46	1.06
S1-100-1	2.47	2.87	0.86	1.48	1.38	1.07	1.14	1.17	0.97	0.78	1.06	0.74
S2-100-1	2.69	2.87	0.94	1.50	1.61	0.93	1.38	1.52	0.91	1.22	1.46	0.84
S3-100-1	2.76	2.87	0.96	2.14	2.02	1.06	1.84	1.96	0.94	1.77	1.92	0.92
S2-50-1	2.78	2.89	0.96	1.72	1.62	1.06	1.59	1.52	1.05	1.39	1.46	0.95
S2-100-0	2.62	2.53	1.04	1.36	1.24	1.10	1.28	1.22	1.05	1.10	1.19	0.92
S2-100-0.5	2.67	2.81	0.95	1.38	1.41	0.98	1.30	1.34	0.97	1.25	1.30	0.96
S2-100-1.5	2.75	2.82	0.98	1.56	1.62	0.96	1.45	1.54	0.94	1.33	1.50	0.89
S2-100-2	2.77	2.89	0.96	1.68	1.85	0.91	1.65	1.74	0.95	1.57	1.67	0.94
N4-0-1	9.62	9.77	0.98	6.31	6.08	1.04	6.04	5.72	1.06	5.85	5.49	1.07
S4-50-1	8.57	9.74	0.88	5.83	6.07	0.96	5.46	5.71	0.96	4.76	5.48	0.87
S4-100-1	8.24	9.69	0.85	5.67	6.04	0.94	5.08	5.69	0.89	4.64	5.46	0.85

370 Note: B_{scr} = the initial flexural stiffness; $B_{s0.5}$, $B_{s0.6}$, and $B_{s0.7}$ = the flexural stiffness when the moment
371 is $0.5M_u$, $0.6M_u$, and $0.7M_u$; B_{exp} = the experimental result of the flexural stiffness; and B_{theo} = the
372 theoretical value of the flexural stiffness.

373 Table 7

374 Load-carrying capacity of beam specimens.

Specimens	$M_{cr}(\text{kN}\cdot\text{m})$			$M_u(\text{kN}\cdot\text{m})$		
	M_{exp}	M_{theo}	M_{exp}/M_{theo}	M_{exp}	M_{theo}	M_{exp}/M_{theo}
N2-0-1	7.65	8.41	0.91	25.27	23.64	1.07
S1-100-1	6.06	7.92	0.77	14.00	13.86	1.01
S2-100-1	6.59	8.63	0.76	21.57	23.54	0.92
S3-100-1	7.44	9.54	0.78	32.56	34.57	0.94
S2-50-1	7.48	8.36	0.89	22.22	23.58	0.94
S2-100-0	3.30	4.39	0.75	20.40	21.82	0.93
S2-100-0.5	5.37	6.21	0.86	20.93	22.80	0.92
S2-100-1.5	6.95	9.99	0.70	21.84	23.68	0.92
S2-100-2	7.98	11.40	0.70	21.65	24.60	0.88
N4-0-1	19.35	20.79	0.93	58.42	55.81	1.05
S4-50-1	19.23	20.68	0.93	54.21	55.66	0.97
S4-100-1	18.96	20.52	0.92	53.19	55.57	0.96

375 Note: M_{cr} = the cracking moment; M_u = the ultimate moment; M_{exp} = the experimental result of the

376 moment; and M_{theo} = the theoretical value of the moment.

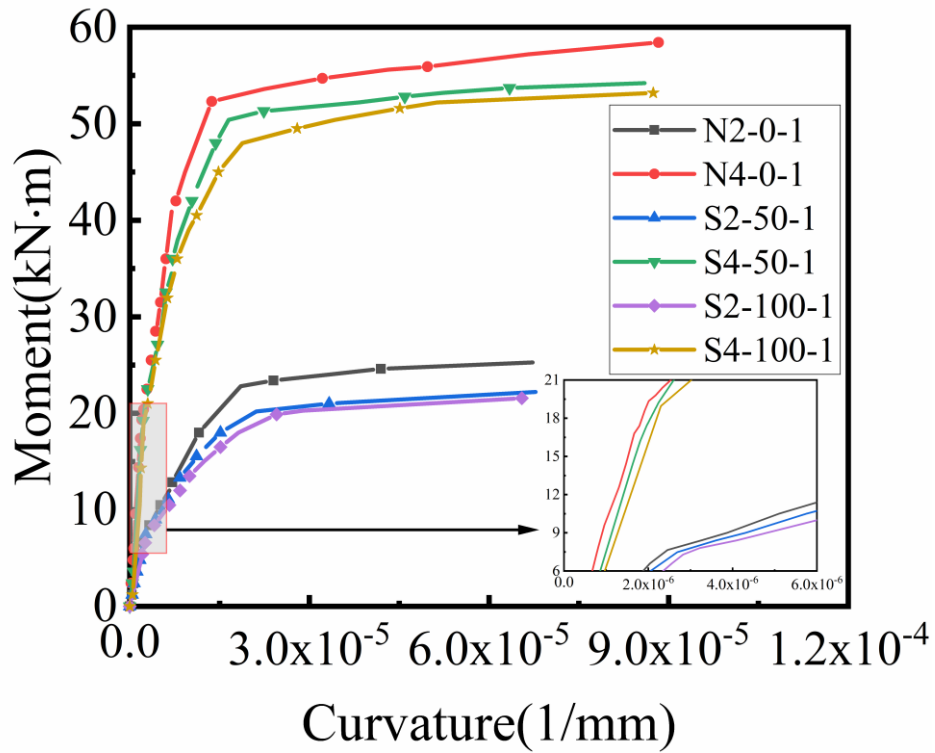
377 Table 8

378 Ductility of beam specimens.

Specimens	$\phi_y(10^{-5}/\text{mm})$	$\phi_u(10^{-5}/\text{mm})$	μ
N2-0-1	1.85	6.72	3.63
S1-100-1	2.23	6.45	2.89

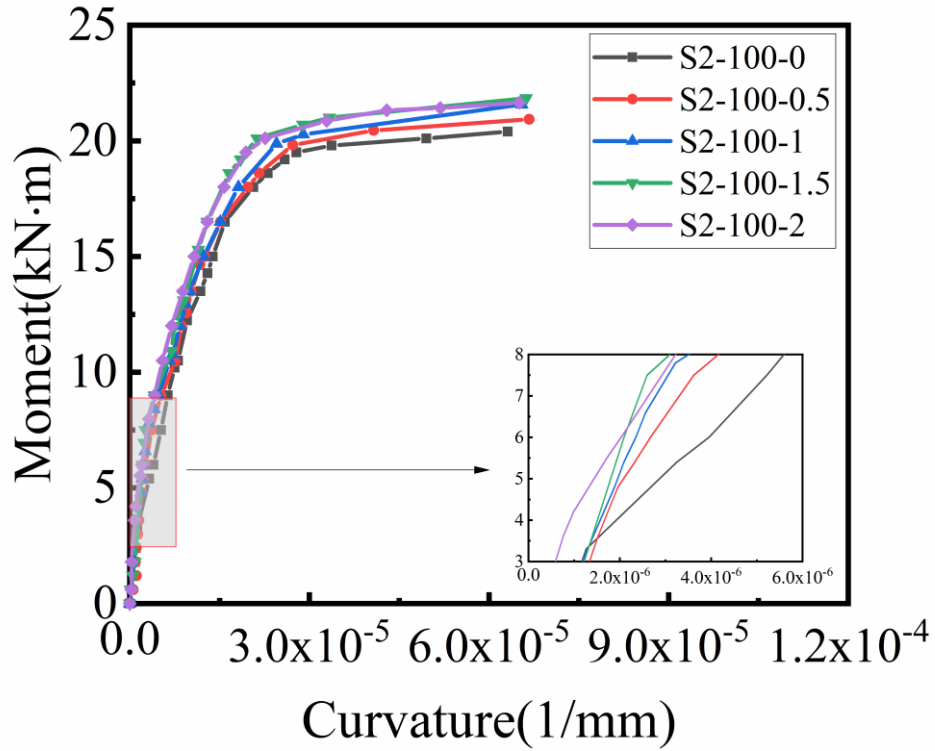
S2-100-1	2.45	6.54	2.67
S3-100-1	2.28	5.95	2.61
S2-50-1	2.11	6.78	3.17
S2-100-0	2.78	6.31	2.26
S2-100-0.5	2.72	6.67	2.45
S2-100-1.5	2.13	6.62	3.10
S2-100-2	1.94	6.50	3.35
N4-0-1	1.37	8.84	6.45
S4-50-1	1.65	8.60	5.21
S4-100-1	1.88	8.74	4.65

379 Note: ϕ_y = the yield curvature; ϕ_u = the ultimate curvature; and μ = the ductility.



380

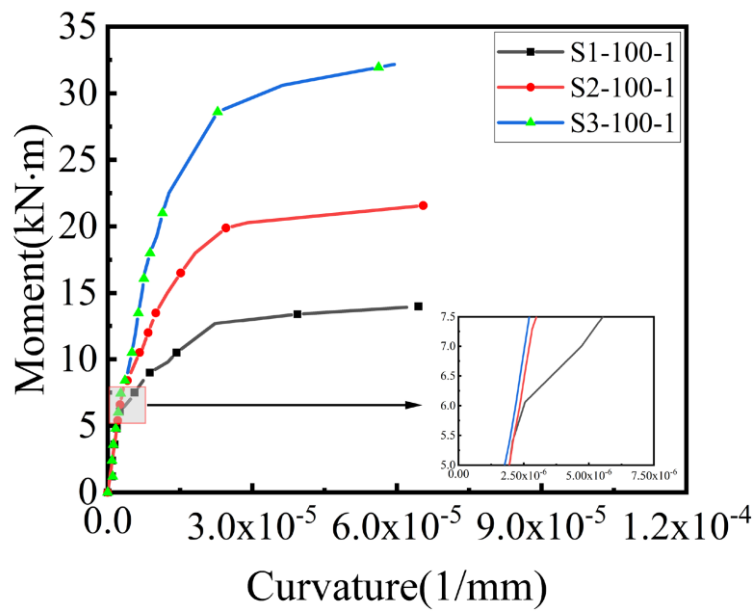
381 (a) Effect of coal gangue replacement rate on the moment-curvature relationships of the beams



382

383

(b) Effect of SFVC on the moment-curvature relationships of the beams



384

385

(c) Effect of rebar ratio on the moment-curvature relationships of the beams

386

Fig. 12. Various effects on the moment-curvature relationships of the beams.

387

4.2. Analysis and calculation of short-term stiffness

388

Considering the effect of steel fibers on structural members, CECS38:2004 (CABR 2004) and

389 GB 50010-2010 (CABR 2011) specify that the flexural stiffness of steel fiber-reinforced concrete
 390 members under flexure is as follows:

$$391 \quad B_{fs} = B_s (1 + \beta_B \lambda_f) \quad (9)$$

$$392 \quad B_s = \frac{E_s A_s h_0^2}{1.15\psi + 0.2 + 6\alpha_E \rho} \quad (10)$$

$$393 \quad \psi = 1.1 - 0.65 \frac{f_{tk}}{\rho_{te} \sigma_s} \quad (11)$$

$$394 \quad \sigma_s = \frac{M}{\eta A_s h_0} \quad (12)$$

$$395 \quad \rho_{te} = \frac{A_s}{0.5bh} \quad (13)$$

396 where λ_f is the characteristic value of the steel fiber content (i.e., $\lambda_f = \rho d_f / d_f$); ρ_f is the SFVC, l_f is the
 397 length of the steel fiber; d_f is the diameter of the steel fiber; β_B is the influence coefficient of the steel
 398 fiber on the short-term stiffness of the steel fiber-reinforced concrete member under flexure, generally
 399 set to 0.35; f_y is the yield strength of the rebar; A_s is the cross-sectional area of the longitudinal rebar;
 400 E_s is the elastic modulus of the rebar; α_E is the ratio of the elastic modulus of the rebar to the elastic
 401 modulus of the concrete; ψ is the coefficient related to the strain heterogeneity of the longitudinal rebar
 402 between cracks; σ_s is the stress in the longitudinal rebar, calculated from $M = 0.5M_u$, $0.6M_u$, and $0.7M_u$
 403 and the corresponding coefficient η (i.e., $\eta = 0.87$); f_{tk} is the tensile strength of the concrete; and ρ_{te} is
 404 the longitudinal rebar ratio calculated from the cross-sectional area of the effective tensile concrete.

405 The initial flexural stiffness is evaluated using $B_{scr} = 0.85E_c I_0$, where E_c is the elastic modulus of
 406 the concrete and I_0 is the moment of inertia of the transformed section. According to GB50010-2010
 407 (CABR 2011), the flexural stiffness under service conditions is estimated using bending moments of
 408 $0.5 M_u$, $0.6 M_u$, and $0.7 M_u$. Table 6 compares the predicted and experimental results of each flexural
 409 stiffness. The ratio of the experimental results to the predicted value is in the range of 0.74-1.11 and

410 the correlation coefficient R^2 is 0.991069, indicating that the predicted results are in good agreement
411 with the experimental results. Therefore, the current design code is applicable for predicting the short-
412 term stiffness of the SFCGC beams under flexure.

413 4.3. Analysis and calculation of crack width

414 4.3.1. Calculation of average crack spacing

415 To the best of our knowledge, a calculation of the average crack spacing of the SFCGC beams
416 has not been reported. The experimental results showed that the number and width of cracks in the
417 SFCGC beams differed from those in the NC beams, mainly due to the low elastic modulus of the
418 lightweight aggregate concrete, which is approximately 25% less than that of conventional concrete
419 of the same grade. In this study, the average crack spacing were calculated using the methods in
420 CECS38:2004 (CABR 2004) and GB 50010-2010 (CABR 2011), as specifically shown in Equation
421 (14). The correlation coefficient in the equation is adjusted by regression fitting of the experimental
422 results.

$$423 \quad l_m = k_1 C_s + k_2 \frac{d_{eq}}{\rho_{te} (1 + \alpha_t \lambda_t)} \quad (14)$$

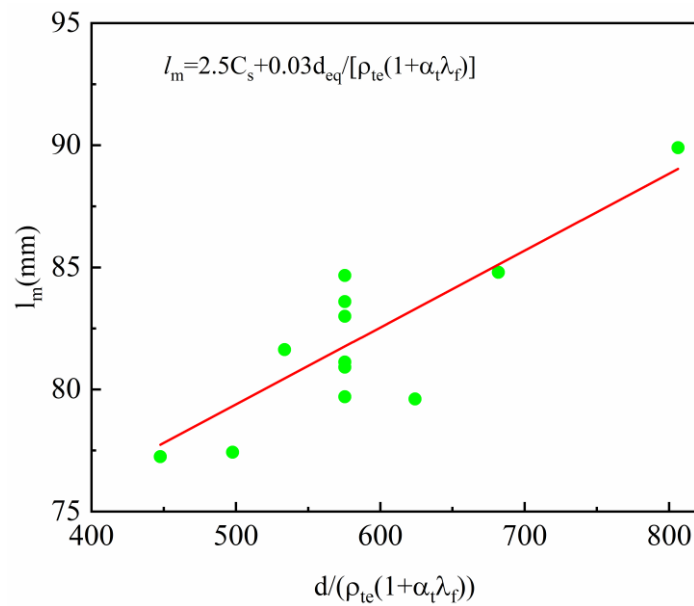
$$424 \quad d_{eq} = \frac{\sum n_i d_i^2}{\sum n_i v_i d_i} \quad (15)$$

425 where α_t is the coefficient of influence of the steel fiber on the tensile strength of the steel fiber-
426 reinforced concrete, which is generally taken as 0.26; d_{eq} is the equivalent diameter of the tensile rebar;
427 C_s is the thickness of the concrete cover of the tensile rebar; d_i is the nominal diameter of the i -th
428 longitudinal rebar in the tension zone; n_i is the number of longitudinal rebar members in the tension
429 zone; and v_i is the relative bond characteristic coefficient of the i -th longitudinal rebar in the tension
430 zone, which is generally taken as 1.0.

431 Through a regression analysis of the experimental results of 12 beams, a fitting curve with d_{eq}/ρ_{te}
 432 as the independent variable and l_m as the dependent variable is obtained, as shown in Fig. 13. The
 433 average crack spacing is calculated using Equation (16):

$$434 \quad l_m = 2.5C_s + 0.03 \frac{d_{eq}}{\rho_{te}(1 + \alpha_t \lambda_f)} \quad (16)$$

435 The experimental results and the values calculated by Equation (16) are shown in Table 9. The
 436 ratio of the experimental results to the predicted value is in the range of 0.98-1.05 and the correlation
 437 coefficient R^2 is 0.999087, indicating that the predicted results are in good agreement with the
 438 experimental results.



439
 440 Fig. 13. Fitted curve of average crack spacing.

441 Table 9

442 Calculated and experimental results of average cracking spacing.

Specimens	$l_{m,exp}/mm$	$l_{m,theo}/mm$	$l_{m,exp}/l_{m,theo}$
N2-0-1	83.60	79.76	1.05
S1-100-1	89.92	86.68	1.04

S2-100-1	79.71	79.76	1.00
S3-100-1	77.25	75.93	1.02
S2-50-1	80.91	79.76	1.01
S2-100-0	84.80	82.95	1.02
S2-100-0.5	79.61	81.22	0.98
S2-100-1.5	81.63	78.51	1.04
S2-100-2	78.82	77.43	1.02
N4-0-1	81.12	79.76	1.02
S4-50-1	82.67	79.76	1.04
S4-100-1	83.00	79.76	1.04

443 Note: $l_{m,exp}$ = the experimental result of the cracking spacing; and $l_{m,theo}$ = the theoretical value of the
444 cracking spacing.

445 4.3.2. Calculation of crack width

446 According to CECS38:2004 (CABR 2004) and GB 50010-2010 (CABR 2011) and the optimized
447 equation for calculating the crack spacing, the average crack width (w_{fm}) can be calculated by Equation
448 (17):

$$449 \quad w_{fm} = (1 - \beta_{cw} \lambda_f) \alpha_c \psi \frac{\sigma_s}{E_s} l_m \quad (17)$$

450 where α_c is the coefficient of influence of the tensile deformation of concrete, which is taken as 0.77
451 according to GB 50010-2010 (CABR 2011); β_{cw} is the coefficient of influence of the steel fibers on
452 the cracks in the steel fiber-reinforced concrete members, which is generally taken as 0.35; and ψ is
453 calculated by Equation (11), and σ_s is calculated using Equation (12).

454 The experimental results and the values calculated by Equation (17) are shown in Table 10. The
 455 ratio of the experimental results to the predicted value is in the range of 0.93-1.05 and the correlation
 456 coefficient R^2 is 0.998921, indicating that the predicted results are in good agreement with the test
 457 results.

458 Table 10

459 Calculated and experimental results of the average crack width.

Specimens	$0.5M_u$			$0.6M_u$			$0.7M_u$		
	w_{exp}	w_{theo}	w_{exp}/w_{theo}	w_{exp}	w_{theo}	w_{exp}/w_{theo}	w_{exp}	w_{theo}	w_{exp}/w_{theo}
N2-0-1	0.044	0.042	1.05	0.059	0.056	1.05	0.068	0.070	0.97
S1-100-1	0.029	0.028	1.04	0.048	0.046	1.04	0.064	0.063	1.02
S2-100-1	0.041	0.042	0.98	0.055	0.056	0.98	0.072	0.070	1.03
S3-100-1	0.042	0.043	0.98	0.057	0.055	1.04	0.068	0.067	1.01
S2-50-1	0.041	0.042	0.98	0.058	0.056	1.04	0.067	0.070	0.96
S2-100-0	0.053	0.055	0.96	0.074	0.071	1.04	0.085	0.087	0.98
S2-100-0.5	0.049	0.050	0.98	0.063	0.066	0.95	0.083	0.081	1.02
S2-100-1.5	0.039	0.041	0.95	0.053	0.054	0.98	0.067	0.066	1.02
S2-100-2	0.032	0.034	0.94	0.044	0.045	0.97	0.059	0.056	1.05
N4-0-1	0.043	0.042	1.02	0.052	0.056	0.93	0.068	0.070	0.97
S4-50-1	0.044	0.042	1.05	0.054	0.056	0.96	0.069	0.070	0.99
S4-100-1	0.041	0.042	0.98	0.058	0.056	1.04	0.071	0.070	1.01

460 Note: w_{exp} = the experimental result of the average crack width; and w_{theo} = the theoretical value of the
 461 average crack width.

462 4.4. Analysis and calculation of bearing capacity

463 4.4.1. Calculation of cracking moment

464 The cracking moment (M_{cr}) of each beam can be obtained according to the cracking load from
465 the test and can also be theoretically calculated by, for example, Equation (18) (Guo and Shi 2003;
466 CABR 2004).

467
$$M_{cr} = \gamma f_{ft} W_0 \quad (18)$$

468
$$\gamma = \left(0.7 + \frac{120}{h} \right) \gamma_m \quad (19)$$

469
$$W_0 = \frac{I_0}{h - x_0} \quad (20)$$

470
$$I_0 = \frac{b}{3} \left[x_0^3 + (h - x_0)^3 \right] + (n - 1) A_s (h_0 - x_0)^2 \quad (21)$$

471
$$x_0 = \left[\frac{1}{2} b h^3 + (n - 1) A_s h_0 \right] / A_0 \quad (22)$$

472
$$f_{ft} = f_{tk} (1 + \alpha_t \lambda_t) \quad (23)$$

473 where f_{ft} is steel fiber-reinforced concrete axial tensile strength; γ is the plastic influence coefficient of
474 the section under flexure; γ_m is the basic value of the plastic influence coefficient of the section under
475 flexure, which is taken as 1.55 according to GB 50010-2010 (CABR 2011); W_0 is the moment of
476 resistance of the section; I_0 is the moment of inertia of the transformed section; A_0 is the transformed
477 cross-sectional area, $A_0 = A_c + (n - 1) A_s$; A_c is the cross-sectional area of the ordinary concrete in the
478 specimen; n is the ratio of the elastic modulus of the rebar to the elastic modulus of the concrete; and
479 x_0 is the depth of the concrete compression zone.

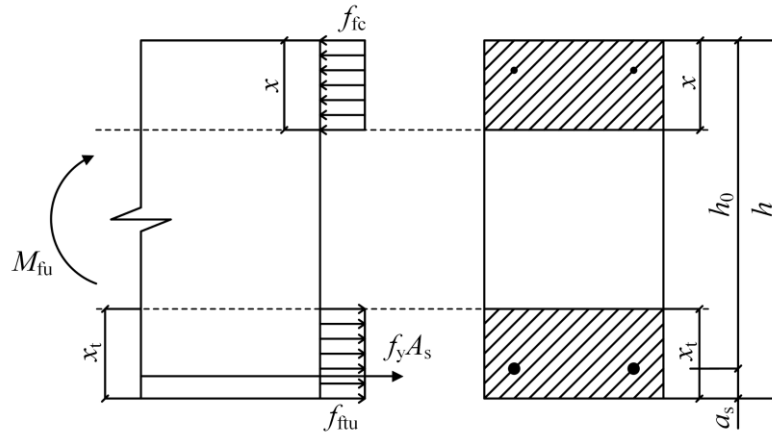
480 The experimental results and the values calculated by Equation (18) are shown in Table 7. The
481 ratio of the experimental results to the predicted value is in the range of 0.70-0.93 and the correlation
482 coefficient R^2 is 0.982778, indicating that the predicted results are in good agreement with the

483 experimental results.

484 4.4.2. Calculation of ultimate moment

485 According to CECS38:2004 (CABR 2004), the ultimate moment (M_u) of the SFCGC beam is

486 calculated by Equation (24), and the calculation diagram is shown in Fig. 14:



487

488

Fig. 14. Calculation diagram of the flexural bearing capacity of the beams.

489

$$M_{f_{iu}} = f_{ic} b x \left(h_0 - \frac{x}{2} \right) - f_{ftu} b x_t \left(\frac{x_t}{2} - a \right) \quad (24)$$

490

$$x = \frac{f_y A_s + f_{ftu} b x_t}{f_{ic} b} \quad (25)$$

491

$$f_{ftu} = f_t \beta_{tu} \lambda_t \quad (26)$$

492 where f_{ic} is the axial compressive strength of the steel fiber-reinforced concrete; f_{ftu} is the tensile

493 strength of the equivalent rectangular stress block of the steel fiber-reinforced concrete in the tension

494 zone; β_{tu} is the coefficient of influence of steel fibers on the tensile effect of the steel fiber concrete in

495 the tension zone in a normal section of the steel fiber-reinforced concrete member, which is taken as

496 1.30 according to the specification; x is the depth of the concrete compression zone, which is assumed

497 to be an equivalent rectangular block; x_t is the depth of the equivalent rectangular stress block in the

498 tension zone, where $x_t = h - x/\beta_1$ with the coefficient β_1 taken as 0.8 for concrete with a strength grade

499 not exceeding C50 according to GB 50010-2010 (CABR 2011); and a is the distance from the resultant
500 point of the longitudinal tensile rebar to the edge of the tension zone of the main section.

501 The experimental results and the values calculated by Equation (24) are shown in Table 7. The
502 ratio of the experimental results to the predicted value is in the range of 0.92-1.07 and the correlation
503 coefficient R^2 is 0.997418, indicating that the predicted results are in good agreement with the
504 experimental results.

505 **5. Parametric Analysis**

506 5.1. Effect of beam depth

507 Fig. 12(a) compares the moment-curvature relationships of beams with different beam depths for
508 the same SFVC (1%) and rebar ratio (almost 1.1%) for each coal gangue replacement rate. As the
509 beam height increases from 200 mm to 300 mm, the load-carrying capacity and flexural stiffness of
510 both the SFCGC and NC beams increase.

511 5.2. Effect of coal gangue replacement rate

512 Fig. 15 exhibits the effects of the coal gangue replacement rate on the flexural stiffness, bending
513 moment, and ductility of the beam specimens with an SFVC of 1% and a rebar ratio of 1.17%. Fig. 15
514 and Tables 6-8 show that with an increase in the coal gangue replacement rate, on average, the initial
515 flexural stiffness and the effective flexural stiffness of the beams decreased by 12% and 11%,
516 respectively, the cracking moment and the ultimate moment decreased by 8% and 13%, respectively,
517 and the ductility decreased by 20%. The coal gangue replacement rate had little effect on the cracking
518 moment and the effective flexural stiffness of the beams but had a significant effect on the initial
519 flexural stiffness because the elastic modulus of the SFCGC was lower than that of the NC.

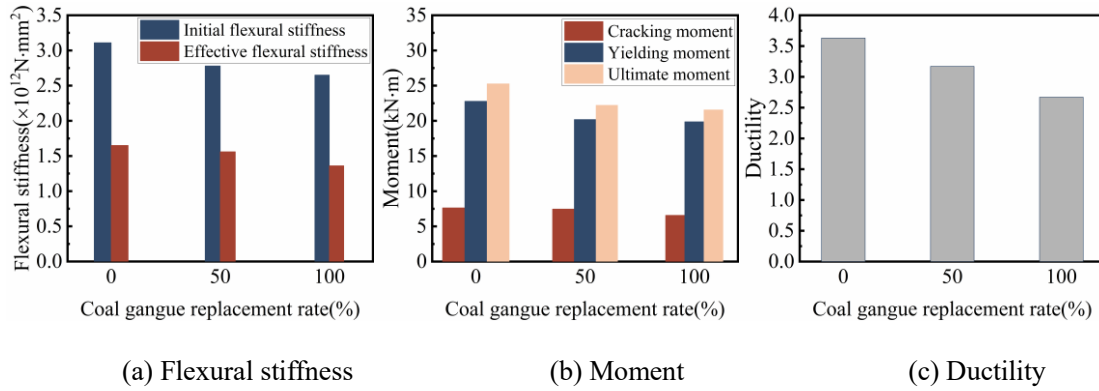


Fig. 15. Effect of coal gangue replacement rate on the flexural behavior of beams.

5.3. Effect of steel fiber volume content

Fig. 16 exhibits the effects of SFVC on the flexural stiffness, bending moment, and ductility of the beam specimens with a coal gangue replacement rate of 100% and a rebar ratio of 1.17%. As seen from Fig. 16 and Tables 6-8, the cracking moment of the SFCGC beams increased by 91% on average compared with that of the beam without steel fibers. This result occurred due to the crack-arresting effect of the steel fibers. The incorporation of steel fibers caused the tensile strength of the SFCGC beams to increase by an average of 39.24% higher on average (Table 3). When the SFVC exceeded 1%, the tensile strength and cracking moment of the SFCGC beams increased nonsignificantly. Hence, the SFVC should not be greater than 1% from the perspective of the optimal utilization of steel fibers. In addition, the SFVC had little effect on the ultimate moment and the initial flexural stiffness of the SFCGC beams, which increased by 5.3% and 3.8% on average, respectively, whereas the effective flexural stiffness and ductility of the SFCGC beams increased by 15.7% and 27.9% on average, respectively, with an increase in the SFVC.

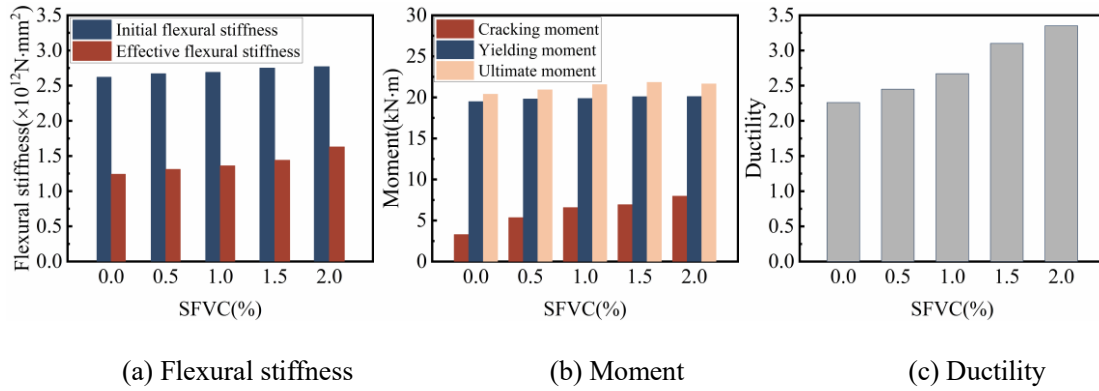


Fig. 16. Effect of SFVC on the flexural behavior of the beams.

5.4. Effect of rebar ratio

Fig. 17 compares the effect of the rebar ratio on the flexural stiffness, bending moment, and ductility of the beam specimens when the coal gangue replacement rate is 100% and the SFVC is 1%.

Fig. 17 shows that the yielding moment and ultimate bending moment of the SFCGC beams increase significantly with the increase in rebar ratio, while the ductility decreases significantly. The rebar ratio has a minimal effect on the initial flexural stiffness, but the effective flexural stiffness is improved by increasing the rebar ratio. With the increase of rebar ratio, the effective flexural stiffness of the SFCGC beams increases by 39.66% on average. The reason is that in the cracking stage of the beam, the initial stiffness of the beam is mainly affected by the elastic modulus of concrete. After the beam cracks, the beam enters the stage of cooperative work between rebar and concrete, so the flexural stiffness of the beam is affected by the performance of the rebar. High rebar ratio is an effective method to improve the bearing capacity and bending stiffness of the SFCGC beams whose strength is lower than that of NC beams.

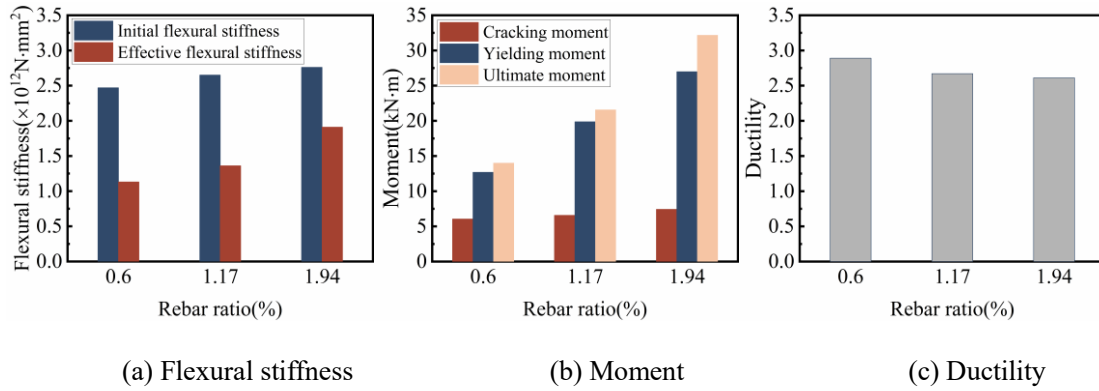


Fig. 17. Effect of rebar ratio on the flexural behavior of the beams.

6. Conclusions

In this study, a simple calculation formula for curvature measurement is proposed, and the current design code formulas for flexural stiffness, crack calculation, cracking moment, and ultimate moment of the SFCGC beams are optimized. And the calculation results are compared with the experimental results. The main conclusions are as follows:

1. In this study, the moment-curvature calculation method is simplified by the knowledge of material mechanics and mathematical theory. The curvature of SFCGC beams can be obtained by measuring the displacement of the SFCGC beams and calculating it, avoiding the need to obtain the curvature of the specimen by measuring concrete strain and steel strain, which greatly reduces the test workload and improves the test efficiency.

2. With the increment of coal gangue replacement rate, the load-carrying capacity of the SFCGC beams decreases compared with the NC beams, but the cracking moment of the SFCGC beams can be improved by incorporating steel fibers, and the ultimate moment of the SFCGC beams by increasing the rebar ratio. The flexural stiffness and ductility of the SFCGC beams increased with the increment of steel fiber volume content. With the increment of rebar ratio, the ultimate moment and flexural stiffness of the SFCGC beams increase substantially but the ductility decreases.

571 3. Based on regression analysis of the experimental results, the equations for calculating the
572 average crack spacing and average crack width of the SFCGC beams were proposed. The calculated
573 results are in good agreement with the experimental results, thereby providing a simple and feasible
574 method for calculating the average crack spacing and average crack width of the SFCGC beams.

575 4. The design methods in current codes predict the SFCGC beams experimental results well in
576 terms of cracking moments, ultimate moments, and flexural stiffness. The mean value of the
577 $M_{cr,exp}/M_{cr,theo}$, $M_{u,exp}/M_{u,theo}$, and B_{exp}/B_{theo} ratio was 0.77, 0.97, and 0.97, respectively. The error
578 between the experimental value and the calculated value was small. This provides a reference for the
579 subsequent theoretical research and practical engineering application of coal gangue concrete
580 components.

581 **Acknowledgments**

582 This research was financially supported by the Foundation of China Scholarship Council (No.
583 201805975002), Jilin Provincial Science and Technology Development Plan Project of China (No.
584 20220203082SF), a scientific research projects from the Education Department of Jilin Province of
585 China (No. JJKH20210279KJ). Guangxi Natrual Science foundation (2021JJA160189), National
586 Natural Science Foundation of China (No. 51968013). Guangxi Natural Science Foundation of (No.
587 2021JJA160189). The authors wish to acknowledge the sponsors. However, any opinions, findings,
588 conclusions and recommendations presented in this paper are those of the authors and do not
589 necessarily reflect the views of the sponsors.

590 **Reference**

591

592

593

594 Atiş, C. D., & Karahan, O. (2009). Properties of steel fiber reinforced fly ash concrete. *Construction*
595 *and Building Materials*, 23(1), 392-399, <http://doi.org/10.1016/j.conbuildmat.2007.11.002>.

596 Babilio, E., & Lenci, S. (2017). On the notion of curvature and its mechanical meaning in a
597 geometrically exact plane beam theory. *International Journal of Mechanical Sciences*, 128,
598 277-293.

599 Brandt, A. M. (2008). Fibre reinforced cement-based (FRC) composites after over 40 years of
600 development in building and civil engineering. *Composite structures*, 86(1-3), 3-9,
601 <http://doi.org/10.1016/j.compstruct.2008.03.006>.

602 CABR (China Academy of Building Research). 2003. Standard for test method of performance on
603 ordinary fresh concrete. (GB/T 50080-2002). China: CABR.

604 CABR (China Academy of Building Research). 2004. Technical specification for fiber reinforced
605 concrete structures (CECS38:2004). China: CABR.

606 CABR (China Academy of Building Research). 2011. Code for design of concrete structures (GB
607 50010-2010). China: CABR.

608 CABR (China Academy of Building Research). 2012. Standard for test methods of concrete structures.
609 (GB/T 50152-2012). China: CABR.

610 CABR (China Academy of Building Research). 2019. Standard for test methods of concrete physical
611 and mechanical properties (GB/T 50081-2019). China: CABR.

612 Cai, B., Li, K., & Fu, F. (2023, June). Flexural behavior of steel fiber-reinforced coal gangue aggregate
613 concrete beams. In *Structures* (Vol. 52, pp. 131-145). Elsevier.

614 <https://doi.org/10.1016/j.istruc.2023.03.172>.

615 Chen, X., Wan, D. W., Jin, L. Z., Qian, K., & Fu, F. (2019). Experimental studies and microstructure
616 analysis for ultra high-performance reactive powder concrete. *Construction and Building*
617 *Materials*, 229, 116924, <https://doi.org/10.1016/j.conbuildmat.2019.116924>.

618 Du, Y., Wang, J., Shi, C., Hwang, H. J., & Li, N. (2021). Flexural behavior of alkali-activat
619 ed slag-based concrete beams. *Engineering Structures*, 229, 111644.

620 Foroughi, S., & Yüksel, S. B. (2020). Investigation of the moment–curvature relationship for
621 reinforced concrete square columns. *Turkish Journal of Engineering*, 4(1), 36-46.

622 Fu, F., Lam, D., Ye, J.(2010), Moment resistance and rotation capacity of semi-rigid composite
623 connections with precast hollowcore slabs, *Journal of Constructional Steel Research*, 2010,
624 66(3), pp. 452–461

625 Fu, F., Parke, G.A.R.(2018), Assessment of the Progressive Collapse Resistance of Double-Layer Grid
626 Space Structures Using Implicit and Explicit Methods , *International Journal of Steel*
627 *Structures*, 2018, 18(3), pp. 831–842

628 Gao, S., Guo, L., Fu, F., Zhang, S.(2017)Capacity of semi-rigid composite joints in accommodating
629 column loss, *Journal of Constructional Steel Research*, 2017, 139, pp. 288–301

630 Gao, S., Zhao, G. H., Guo, L. H., Zhou, L. Q., & Yuan, K. K. (2021). Utilization of coal gangue as
631 coarse aggregates in structural concrete. *Construction and Building Materials*, 268, 121212,
632 <https://doi.org/10.1016/j.conbuildmat.2020.121212>.

633 Gong, C., Yan, J., Liu, J., & Yu, H. (2016). Biology Migration and Distribution Characteristics of Trace
634 Elements in Reconstructed Soil with Coal Gangue Filling. *Agricultural Science &*
635 *Technology*, 17(9), 2167.

636 Guo, J. M., & Zhu, L. L. (2011). Experimental research on durabilities of coal gangue conc
637 rete. In *Advanced Materials Research* (Vol. 306, pp. 1569-1575). Trans Tech Public
638 ations Ltd, <https://doi.org/10.4028/www.scientific.net/AMR.306-307.1569>.

639 Guo, Y., Yan, K., Cui, L., & Cheng, F. (2016). Improved extraction of alumina from coal gangue by
640 surface mechanically grinding modification. *Powder Technology*, 302, 33-41,
641 <http://dx.doi.org/10.1016/j.powtec.2016.08.034>.

642 Guo, Z. H., & Shi, X. D. (2003) Reinforced concrete theory and analyse. *Tsinghua University Press*.
643 (in Chinese)

644 Hadhood, A., Mohamed, H. M., & Benmokrane, B. (2018). Flexural stiffness of GFRP-and CFRP-RC
645 circular members under eccentric loads based on experimental and curvature analysis. *ACI*
646 *Struct. J*, 115(4), 1185-1198.

647 Hasan, H. A., Karim, H., Sheikh, M. N., & Hadi, M. N. (2019). Moment-curvature behavior of glass
648 fiber-reinforced polymer bar-reinforced normal-strength concrete and high-strength
649 concrete columns. *ACI Structural Journal*, 116(4), 65-75.

650 Jabłońska, B., Kityk, A. V., Busch, M., & Huber, P. (2017). The structural and surface prop
651 erties of natural and modified coal gangue. *Journal of environmental management*,
652 190, 80-90, <https://doi.org/10.1016/j.jenvman.2016.12.055>.

653 Jia, J., Cao, Q., Zhang, L., & Zhou, J. (2021). Flexural performance of reinforced concrete
654 beams made by innovative post-filling coarse aggregate process. *Advances in Struct*
655 *ural Engineering*, 24(13), 2898-2911.

656 Jin-min, G. (2011, May). Experimental research on performances of concrete with coal gang
657 ue. In *2011 International Conference on Materials for Renewable Energy & Enviro*

658 nment (Vol. 2, pp. 1988-1991). IEEE, 10.1109/ICMREE.2011.5930728.

659 Karimaei, M., Dabbaghi, F., Sadeghi-Nik, A., & Dehestani, M. (2020). Mechanical performance of
660 green concrete produced with untreated coal waste aggregates. *Construction and Building*
661 *Materials*, 233, 117264, <https://doi.org/10.1016/j.conbuildmat.2019.117264>.

662 Katzer, J., & Domski, J. (2012). Quality and mechanical properties of engineered steel fibres used as
663 reinforcement for concrete. *Construction and Building Materials*, 34, 243-248,
664 <http://dx.doi.org/10.1016/j.conbuildmat.2012.02.058>.

665 Kwak, H. G., & Kim, S. P. (2002). Nonlinear analysis of RC beams based on moment–curvature
666 relation. *Computers & structures*, 80(7-8), 615-628.

667 Li, D., Song, X., Gong, C., & Pan, Z. (2006). Research on cementitious behavior and mech
668 anism of pozzolanic cement with coal gangue. *Cement and Concrete Research*, 36
669 (9), 1752-1759, <https://doi.org/10.1016/j.cemconres.2004.11.004>.

670 Li, Y., Yao, Y., Liu, X. M., Sun, H. H., & Ni, W. (2013). Improvement on pozzolanic reactivity of coal
671 gangue by integrated thermal and chemical activation. *Fuel*, 109, 527-533,
672 <http://dx.doi.org/10.1016/j.fuel.2013.03.010>.

673 Liu, H. Q., Xu, Q., Wang, Q. H., & Zhang, Y. Z. (2020). Prediction of the elastic modulus of concrete
674 with spontaneous-combustion and rock coal gangue aggregates, *Structures*, 28, 774-785,
675 <https://doi.org/10.1016/j.istruc.2020.09.021>.

676 Ma, H. Q., Yi, C., Zhu, H. G., Dong, Z. C., Chen, H. Y., Wang, J. X., & Li, D. Y. (2018). Compressive
677 strength and durability of coal gangue aggregate concrete. *Mater. Rep. B*, 32, 2390-2395,
678 <http://doi.org/10.11896/j.issn.1005-023X.2018.14.012>.

679 Ma, H. Q., Zhu, H. G., Wu, C., Chen, H. Y., Sun, J. W., & Liu, J. Y. (2020). Study on compressive

680 strength and durability of alkali-activated coal gangue-slag concrete and its
681 mechanism. *Powder Technology*, 368, 112-124,
682 <https://doi.org/10.1016/j.powtec.2020.04.054>.

683 Moghadam, M. J., Ajalloeian, R., & Hajiannia, A. (2019). Preparation and application of alkali-
684 activated materials based on waste glass and coal gangue: A review. *Construction and*
685 *Building Materials*, 221, 84-98, <https://doi.org/10.1016/j.conbuildmat.2019.06.071>.

686 Mohammadi, Y., Singh, S. P., & Kaushik, S. K. (2008). Properties of steel fibrous concrete containing
687 mixed fibres in fresh and hardened state. *Construction and Building Materials*, 22(5), 956-
688 965, <https://doi.org/10.1016/j.conbuildmat.2006.12.004>.

689 Olivito, R. S., & Zuccarello, F. A. (2010). An experimental study on the tensile strength of steel fiber
690 reinforced concrete. *Composites Part B: Engineering*, 41(3), 246-255,
691 <https://doi.org/10.1016/j.compositesb.2009.12.003>.

692 Priestley, M. J. N., Park, R., & Lu, F. P. S. (1971). Moment-curvature relationships for prestressed
693 concrete in constant-moment zones. *Magazine of Concrete Research*, 23(75-76), 69-78.

694 Qian K, Geng SY, Liang SL, Fu F, Yu J,(2022) Effects of loading regimes on the structural behavior
695 of RC beam-column sub-assemblages against disproportionate collapse, *Engineering*
696 *Structures* 251, 113470

697 Qian K, Lan,DQ, Fu, F, Li B (2020), Effects of infilled wall opening on load resisting capacity of RC
698 frames to mitigate progressive collapse risk, *Engineering Structures* 223, 111196

699 Qian K, Liang SL, Feng DC, Fu F, Wu G (2020), Experimental and numerical investigation on
700 progressive collapse resistance of post-tensioned precast concrete beam-column sub-
701 assemblages, *Journal of Structural Engineering* 146 (9)

702 Qian K, Weng YH ,Fu,, F, Deng XF (2021), Numerical evaluation of the reliability of using single-
703 story substructures to study progressive collapse behaviour of multi-story RC frames ,
704 *Journal of Building Engineering* 33, 101636

705 Qin, J. G., Zhao, R. D., Chen, T. J., Zi, Z. Y., & Wu, J. H. (2019). Co-combustion of municipal solid
706 waste and coal gangue in a circulating fluidized bed combustor. *International Journal of*
707 *Coal Science & Technology*, 6(2), 218-224, <http://doi.org/10.1007/s40789-018-0231-4>.

708 Qin, L., & Gao, X. (2019). Properties of coal gangue-Portland cement mixture with carbonat
709 ion. *Fuel*, 245, 1-12, <https://doi.org/10.1016/j.fuel.2019.02.067>.

710 Schreier, H., Orteu, J. J., & Sutton, M. A. (2009). *Image correlation for shape, motion and deformation*
711 *measurements: Basic concepts, theory and applications* (Vol. 1). Boston, MA: Springer-
712 Verlag US, <https://doi.org/10.1007/978-0-387-78747-3>.

713 Sun, Y. X., & Li, X. D. (2011). Development and design of coal gangue concrete filling material. In
714 *Advanced Materials Research* (Vol. 295, pp. 1198-1201). Trans Tech Publications Ltd,
715 <https://doi.org/10.4028/www.scientific.net/AMR.295-297.1198>.

716 Viet, N. V., & Zaki, W. (2019). Analytical investigation of the behavior of concrete beams reinforced
717 with multiple circular superelastic shape memory alloy bars. *Composite Structures*, 210,
718 958-970.

719 Wang, L., Shen, N., Zhang, M., Fu, F., & Qian, K. (2020). Bond performance of Steel-CFRP bar
720 reinforced coral concrete beams. *Construction and Building Materials*, 245, 118456.

721 Wang, Z., & Zhao, N. (2015). Influence of coal gangue aggregate grading on strength properties of
722 concrete. *Wuhan University Journal of Natural Sciences*, 20(1), 66-72,
723 <https://doi.org/10.1007/s11859-015-1060-6>.

- 724 Wu, J., Bai, G. L., Wang, P., & Liu, Y. (2018). Mechanical properties of a new type of block made
725 from shale and coal gangue. *Construction and Building Materials*, *190*, 796-804,
726 <https://doi.org/10.1016/j.conbuildmat.2018.09.130>.
- 727 Wu, T., Sun, Y., Liu, X., & Cao, Y. (2021). Comparative study of the flexural behavior of steel fiber-
728 reinforced lightweight aggregate concrete beams reinforced and prestressed with CFRP
729 tendons. *Engineering Structures*, *233*, 111901.
- 730 Yazıcı, Ş., İnan, G., & Tabak, V. (2007). Effect of aspect ratio and volume fraction of steel fiber on the
731 mechanical properties of SFRC. *Construction and Building Materials*, *21*(6), 1250-1253,
732 <http://doi.org/10.1016/j.conbuildmat.2006.05.025>.
- 733 Zhang, Y. Z., Wang, Q. H., Zhou, M., Fang, Y. F., & Zhang, Z. K. (2020). Mechanical properties of
734 concrete with coarse spontaneous combustion gangue aggregate (SCGA): experimental
735 investigation and prediction methodology. *Construction and Building Materials*, *255*,
736 119337, <https://doi.org/10.1016/j.conbuildmat.2020.119337>.
- 737 Zhu, H., Yang, S., Li, W., Li, Z., Fan, J., & Shen, Z. (2020). Study of mechanical properties and
738 durability of alkali-activated coal gangue-slag concrete. *Materials*, *13*(23), 5576,
739 <https://doi.org/10.3390/ma13235576>.